VOLUME 28, ISSUES 1–3, 2009   ISSN 1463–5003

ELSEVIER

OCEAN MODELLING

http://www.elsevier.com/locate/ocemod

Editor-in-Chief: **Will Perrie,**
*Bedford Institute of Oceanography,
Nova Scotia, Canada*

Special Issue

The Sixth International Workshop on Unstructured
Mesh Numerical Modelling of Coastal,
Shelf and Ocean Flows

Guest Editors

Emmanuel Hanert, David Ham, Julie Pietrzak,
Jens Schröter and Chris Pain

A tale of two elements: $P_1^{NC} - P_1$ and RT_0

Emmanuel Hanert [a,*], Roy A. Walters [b], Daniel Y. Le Roux [c], Julie D. Pietrzak [d]

[a] Department of Meteorology, The University of Reading, Earley Gate, P.O. Box 243, Reading RG6 6BB, UK
[b] 6051 Hunt Road, Victoria, BC, V8Y 3H7, Canada
[c] Département de Mathématiques et de Statistique, Université Laval, Québec, QC, G1K 7P4, Canada
[d] Faculteit CiTG, TU Delft, Stevinweg 1, 2628 CN Delft, The Netherlands

A B S T R A C T

The $P_1^{NC} - P_1$ and RT_0 finite element schemes are among the most promising low order elements for use in unstructured mesh marine and lake models. They are both free of spurious elevation modes, have good dispersive properties and have a relatively low computational cost. In this paper, we derive both finite element schemes in the same unified framework and discuss their respective qualities in terms of conservation, consistency, propagation factor and convergence rate. We also highlight the impact that the local variables placement can have on the model solution. The main conclusion that we can draw is that the choice between elements is highly application dependent. We suggest that the $P_1^{NC} - P_1$ element is better suited to purely hydrodynamical applications while the RT_0 element might perform better for hydrological applications that require scalar transport calculations.

Crown Copyright © 2008 Published by Elsevier Ltd. All rights reserved.

1. Introduction

In the last 10 years, there has been an on-going effort to develop a new generation of marine models using unstructured rather than structured meshes. Several numerical methods have been investigated such as the finite element (FE), finite volume and spectral element methods. Among these three families of numerical methods, the FE method is the more general as the finite volume and spectral element methods can be seen as discontinuous and high order FE methods, respectively.

The late application of the finite element method to simulate marine flows is partly due to the issue of computational pressure modes, which were found to be present in most of the initial FE models and rendered them inaccurate (Walters and Carey, 1983; Walters, 1983; Walters and Carey, 1984). The approach originally proposed to avoid these modes was to use a modified form of the governing equation that does not support them. This method, called the wave equation method (Lynch and Gray, 1979), allows to use simple low order elements and accurately solves non-dispersive wave propagation problems. However, the wave equation formulation appears to be subject to advective instabilities and presents mass conservation issues (Kolar et al., 1994; Massey and Blain, 2006). The shortcomings of the wave equation formulation therefore lead to more research on finite element pairs to solve

the primitive equations without having recourse to modified formulations or stabilization. Among the family of low order FE pairs, the $P_1^{NC} - P_1$ and RT_0 elements have appeared to have most of the desired qualities, i.e., absence of spurious modes, simplicity and good dispersive properties.

The lowest order Raviart–Thomas element (Raviart and Thomas, 1977), RT_0, tries to mimic the finite difference C-grid. Like the C-grid, the RT_0 element has spurious *f*-modes in the velocity but no spurious elevation modes (Raviart and Thomas, 1977; Hanert et al., 2003; Le Roux et al., 2007). However, there is usually no significant development of these modes so they are not an issue as long as the Rossby deformation radius is well resolved. The RT_0 FE scheme has been used in the unstructured mesh models developed by Walters and Casulli (1998) and Miglio et al. (1999). Other models based on a finite volume or finite difference formalism but using the same variables placement as the RT_0 element have also been developed (Casulli and Walters, 2000; Chen et al., 2003; Ham et al., 2005; Walters, 2005; Fringer et al., 2006; Stuhne and Peltier, 2006). The success of RT_0 is partly due to its formulation that has similarities with finite volumes although it is not a finite volume scheme.

The linear non-conforming, conforming element, $P_1^{NC} - P_1$, does not really have an equivalent Arakawa-type finite difference grid but has some similarities with the CD-grid of Adcroft et al. (1999) with the exception that the elevation lies on the vertices rather than at the center of the elements (Le Roux, 2005). The $P_1^{NC} - P_1$ has first been used by Hua and Thomasset (1984) to solve the shallow-water equations but then laid dormant for about 20 years before it was analysed by Le Roux (2005) and used by Hanert

* Corresponding author.
E-mail addresses: e.a.hanert@reading.ac.uk (E. Hanert), rawalters@shaw.ca (R.A. Walters), Daniel.Leroux@mat.ulaval.ca (D.Y. Le Roux), J.D.Pietrzak@tudelft.nl (J.D. Pietrzak).

et al. (2005) to solve the non-linear shallow water equations. The $P_1^{NC} - P_1$ element has since then been used in unstructured mesh models developed by Greenberg et al. (2007), Sobolev et al. (2007), White et al. (2008a) and Lambrechts et al. (2008).

Although further developments should certainly be expected in the future, especially among fully discontinuous low and high order elements (Bernard et al., 2007; Giraldo and Warburton, 2008), here we present both FE pairs within an unified framework. This is the first time such a comparison has been made and it allows us to highlight their differences and similarities. In turn this allows us to make some recommendations regarding their domain of applicability. Given the widespread interest in this class of FE methods we believe this is of broad interest to not only the ocean modelling community but also to the limnology community as well. Both communities are actively developing these types of numerical solution techniques.

As usual for such comparative studies, we take the shallow water equations model as a benchmark problem. After having derived the discrete formulations for both elements in Section 2, we shall discuss their respective qualities by considering their propagation factors (Section 3), conservation properties (Section 4), convergence rates (Section 5) and the effects of different approximations (section 6). We conclude with recommendations concerning the types of problems for which they are best suited.

2. Formulation

The model equations are the two-dimensional shallow water equations. These equations are derived by vertically integrating the Reynolds-averaged Navier–Stokes equations and using the hydrostatic assumption and the Boussinesq approximation. The continuity and momentum equations are

$$\frac{\partial \eta}{\partial t} + \mathbf{\nabla} \cdot (H\mathbf{u}) = 0, \tag{1}$$

$$\frac{D\mathbf{u}}{Dt} + f\mathbf{e}_z \times \mathbf{u} + g\mathbf{\nabla}\eta + \mathscr{D} - \mathscr{T} = 0, \tag{2}$$

where $\mathbf{u}(\mathbf{x},t)$ is the depth-averaged horizontal velocity with components (u,v), f is the Coriolis parameter, $\mathbf{e}_z$ is the upward unit vector, g is the gravitational acceleration, $H = h + \eta$ is the total water depth, $h(\mathbf{x})$ is the water depth measured from a reference elevation, $\eta(\mathbf{x},t)$ is the distance from the reference elevation to the free surface, $\mathscr{D}$ and $\mathscr{T}$ are dissipation and forcing terms, $\mathbf{x} = (x,y)$ is the horizontal coordinate, $\frac{D}{Dt} = \frac{\partial}{\partial t} + \mathbf{u} \cdot \mathbf{\nabla}$ is the material derivative and $\mathbf{\nabla} = \left(\frac{\partial}{\partial x}, \frac{\partial}{\partial y}\right)$ is the horizontal gradient.

No-normal flow boundary conditions are imposed on the boundary of the domain Ω ($\mathbf{u} \cdot \mathbf{n} = 0$ on $\partial\Omega$, where $\mathbf{n}$ is the unit normal vector), which is assumed to be closed. Depending on the order of the dissipation term, some additional boundary conditions might be needed. These do generally not pose a problem and we will assume that the no-normal flow boundary condition is sufficient to find a unique solution. In the first part of the paper, we are going to use only the linearised shallow water equations, i.e., the elevation is neglected in front of the water depth in the continuity equation ($H = h$) and advection is neglected in the momentum equation. We shall only use the non-linear equations in Section 6.

2.1. Weak formulations

In order to obtain the finite element discretization of the linearised version of Eqs. (1) and (2), we first have to derive their weak formulation on the computational domain Ω. The latter is obtained by multiplying Eq. (1) and (2) by test functions $\hat{\eta}$ and $\hat{\mathbf{u}}$ and then integrating on Ω:

$$\int_\Omega \frac{\partial \eta}{\partial t}\hat{\eta}d\Omega + \int_\Omega \mathbf{\nabla} \cdot (h\mathbf{u})\hat{\eta}d\Omega = 0, \tag{3}$$

$$\int_\Omega \frac{\partial \mathbf{u}}{\partial t} \cdot \hat{\mathbf{u}}d\Omega + \int_\Omega f(\mathbf{e}_z \times \mathbf{u}) \cdot \hat{\mathbf{u}}d\Omega + g\int_\Omega \mathbf{\nabla}\eta \cdot \hat{\mathbf{u}}d\Omega$$
$$+ \int_\Omega (\mathscr{D} - \mathscr{T}) \cdot \hat{\mathbf{u}}d\Omega = 0, \tag{4}$$

$\forall\hat{\eta} \in \mathscr{H}$ and $\forall\hat{\mathbf{u}} \in \mathscr{U}$, where $\mathscr{H}$ and $\mathscr{U}$ are functional spaces defined later. In order to only have space derivatives of functions in $\mathscr{H}$ or in $\mathscr{U}$, we may integrate by parts either the divergence or the gradient term. Hence we respectively obtain the following weak formulations:

$$\boxed{\begin{array}{l} \text{Find } \eta(\mathbf{x},t) \in \mathcal{H} \text{ and } \mathbf{u}(\mathbf{x},t) \in \mathcal{U} \text{ such that} \\[1em] < \frac{\partial \eta}{\partial t}\hat{\eta} > - < h\mathbf{u} \cdot \mathbf{\nabla}\hat{\eta} > + \ll \hat{\eta}h\mathbf{u} \cdot \mathbf{n} \gg = 0 \\[1em] < \frac{\partial \mathbf{u}}{\partial t} \cdot \hat{\mathbf{u}} > + < f(\mathbf{e}_z \times \mathbf{u}) \cdot \hat{\mathbf{u}} > + g < \mathbf{\nabla}\eta \cdot \hat{\mathbf{u}} > \\[0.5em] \qquad + < (\mathcal{D} - \mathcal{T}) \cdot \hat{\mathbf{u}} > = 0 \\[1em] \hfill \forall\hat{\eta} \in \mathcal{H}, \ \forall\hat{\mathbf{u}} \in \mathcal{U}, \end{array}} \tag{5}$$

and

$$\boxed{\begin{array}{l} \text{Find } \eta(\mathbf{x},t) \in \mathcal{H} \text{ and } \mathbf{u}(\mathbf{x},t) \in \mathcal{U} \text{ such that} \\[1em] < \frac{\partial \eta}{\partial t}\hat{\eta} > + < \mathbf{\nabla} \cdot (h\mathbf{u})\hat{\eta} > = 0 \\[1em] < \frac{\partial \mathbf{u}}{\partial t} \cdot \hat{\mathbf{u}} > + < f(\mathbf{e}_z \times \mathbf{u}) \cdot \hat{\mathbf{u}} > - g < \eta\mathbf{\nabla} \cdot \hat{\mathbf{u}} > + g \ll \eta\hat{\mathbf{u}} \cdot \mathbf{n} \gg \\[0.5em] \qquad + < (\mathcal{D} - \mathcal{T}) \cdot \hat{\mathbf{u}} > = 0 \\[1em] \hfill \forall\hat{\eta} \in \mathcal{H}, \ \forall\hat{\mathbf{u}} \in \mathcal{U}, \end{array}} \tag{6}$$

where $\langle . \rangle = \int_\Omega . d\Omega$ and $\ll . \gg = \int_{\partial\Omega} . d\Gamma$. It should be noted that the impermeability boundary conditions can be naturally incorporated in formulation (5) by setting the boundary integral to zero. With that formulation, it is possible to select a functional space $\mathscr{U}$ containing only functions that either satisfy the boundary conditions or not. In other words, we can decide to impose the no-normal flow constraint only in a weak way (as typically natural boundary conditions are imposed in second order problems) or in the usual strong way thanks to an additional constraint on the functional space (Hanert and Legat, 2006).

Formulations (5) and (6) have been obtained from the model Eqs. (1) and (2) without making any assumptions about the numerical schemes that will be used to solve these equations. The solution to formulation (5) belongs to the functional spaces $\mathscr{H} = H^1(\Omega)$ and $\mathscr{U} = (L^2(\Omega))^2$ while the solution to formulation (6) belongs to $\mathscr{H} = L^2(\Omega)$ and $\mathscr{U} = H(\text{div}, \Omega) \equiv \{\mathbf{v}|\mathbf{v} \in (L^2(\Omega))^2 \text{ and } \mathbf{\nabla} \cdot \mathbf{v} \in L^2(\Omega)\}$.

2.2. Finite element discretizations

A finite element approximation to the exact solution of Eqs. (1) and (2) is found by replacing η and $\mathbf{u}$ by finite element approximations η^h and $\mathbf{u}^h$ in formulation (5) or (6). Those approximations respectively belong to finite dimensional spaces $\mathscr{H}^h \subset \mathscr{H}$ and $\mathscr{U}^h \subset \mathscr{U}$. They read

$$\eta \approx \eta^h = \sum_{i=1}^M \eta_i \phi_i,$$

$$\mathbf{u} \approx \mathbf{u}^h = \sum_{j=1}^N \mathbf{u}_j \psi_j \text{ or } \sum_{j=1}^N J_j \tau_j,$$

where η_i, $\mathbf{u}_j$ and J_j represent elevation, vectorial velocity and normal velocity nodal values, and ϕ_i, ψ_j and τ_j represent the elevation, scalar velocity and vectorial velocity shape functions. Since the velocity is a vectorial quantity, there are two possible finite element approximations. One is to use vectorial velocity nodal values and scalar basis functions, while the other amounts to use scalar degrees of freedom and vectorial basis functions. The former will be used for the $P_1^{NC} - P_1$ scheme and the latter for the RT_0 scheme.

Nodal values and shape functions are associated with a triangulation of the computational domain Ω into N_E disjoint elements E_e. The total number of vertices and segments in the triangulation are respectively denoted N_V and N_S. The shape functions ϕ_i, ψ_j and τ_j are piecewise polynomials (not necessary of the same degree) spanning the finite dimensional spaces $\mathscr{H}^h$ and $\mathscr{U}^h$. Nodal values are found by applying the Galerkin procedure which amounts to replace $\hat{\eta}$ by ϕ_i and $\hat{\mathbf{u}}$ by $(\psi_j, 0)$ and $(0, \psi_j)$ or by τ_j in the weak formulation for $1 \leqslant i \leqslant M$ and $1 \leqslant j \leqslant N$.

In this paper, we aim to compare the $P_1^{NC} - P_1$ and RT_0 finite element schemes. The former element has a linear conforming (P_1) representation of surface elevation and a linear non-conforming (P_1^{NC}) representation of the velocity. Both shape functions are scalar and are shown in Fig. 1. Nodal values associated with a linear conforming approximation are located on the vertices of the mesh whereas non-conforming nodal values lie at mid-segments ($M = N_V$, $N = 2N_S$). Since there is only one common node between two adjacent triangles, a linear non-conforming approximation is discontinuous across triangle boundaries except at mid-side nodes. A conforming approximation is continuous everywhere. Note that the non-conforming finite element space is not a subspace of $H(\mathrm{div}, \Omega)$. As result, formulation (6) cannot be used to derive the discrete equations. However, formulation (5) can be used as the $P_1^{NC} - P_1$ approximation of the velocity and elevation belongs to $(L^2(\Omega))^2 \times H^1(\Omega)$.

The RT_0 element uses piecewise constant and piecewise linear approximations for the elevation and velocity, respectively. Elevation nodal values are located at elements centroids while velocity nodal values lie at mid-segments ($M = N_E$, $N = N_S$). Velocity degrees of freedom are scalar and the corresponding shape functions are therefore vectorial. The velocity nodal value J_i at a given node i is equal to the normal velocity to the edge Γ_i. On a given element E_e of the triangulation, the restriction of the dimensionless vector shape function τ_i is given by

$$\tau_i(\mathbf{x})|_{E_e} = \frac{\mathbf{x} - \mathbf{x}_i}{2d_i},$$

where d_i is the normal distance from edge i to $\mathbf{x}_i$ and $\mathbf{x}_i$ is the coordinate of the vertex i opposite to the edge Γ_i. RT_0 velocity shape functions have the following properties:

$$\nabla \cdot \tau_i|_{E_e} = \frac{1}{d_i},$$

$$\tau_i|_{E_e} \cdot \mathbf{n}_m = \delta_{im},$$

where $\mathbf{n}_m$ is the outward normal to the edge Γ_m. Since the RT_0 approximation of the velocity and elevation belongs to $H(\mathrm{div}, \Omega) \times L^2(\Omega)$, formulation (6) is used to derive the discrete equations.

The final set of semi-discrete equations may be written as

$$\mathsf{M}_{ij}^{\eta} \frac{\mathrm{d}}{\mathrm{d}t} \mathsf{E}_j + \mathsf{D}_{ij} \mathsf{U}_j = 0, \tag{7}$$

$$\mathsf{M}_{ij}^u \frac{\mathrm{d}}{\mathrm{d}t} \mathsf{U}_j + \mathsf{C}_{ij} \mathsf{U}_j + \mathsf{G}_{ij} \mathsf{E}_j = \mathsf{R}_j, \tag{8}$$

where it is assumed that there is a sum on repeated indices. The nodal values vectors E and U, and the matrices M^{η}, M^u, C, G and D are defined as follows for the two elements:

	$P_1^{NC} - P_1$	RT_0
U	$\begin{pmatrix} u_i \\ v_i \end{pmatrix}$	$\begin{pmatrix} J_j \end{pmatrix}$
E	$\begin{pmatrix} \eta_j \end{pmatrix}$	$\begin{pmatrix} \eta_j \end{pmatrix}$
M^{η}	$\left(<\phi_i^1 \phi_j^1> \right)$	$\left(<\phi_i^0 \phi_j^0> \right)$
M^u	$\left(\begin{array}{c\|c} <\psi_i^1 \psi_j^1> & 0 \\ \hline 0 & <\psi_i^1 \psi_j^1> \end{array} \right)$	$\left(<\tau_i^1 \cdot \tau_j^1> \right)$
C	$\left(\begin{array}{c\|c} 0 & -<f\psi_i^1 \psi_j^1> \\ \hline <f\psi_i^1 \psi_j^1> & 0 \end{array} \right)$	$\left(<f\tau_i^1 \cdot (\mathbf{e}_z \times \tau_j^1)> \right)$
G	$\begin{pmatrix} -g<\psi_i^1 \phi_{j,x}^1> \\ -g<\psi_i^1 \phi_{j,y}^1> \end{pmatrix}$	$g\left(<\nabla \cdot \tau_i^1 \phi_j^0> \right)$
D	$\left(<h\phi_{i,x}^1 \psi_j^1> \mid <h\phi_{i,y}^1 \psi_j^1> \right)$	$\left(-<\phi_i^0 \nabla \cdot (h\tau_j^1)> \right)$

Note that the superscripts "0" and "1" have been used to indicate the degree of the shape functions. In the case of a constant bathymetry, the divergence matrix simply reads

$$\mathsf{D} = -\frac{h}{g} \mathsf{G}^T.$$

The right-hand-side vector R contains the dissipation and forcing components. It is worth noting that the RT_0 elevation mass matrix and the $P_1^{NC} - P_1$ velocity mass matrix are diagonal. Furthermore the RT_0 Coriolis matrix is uniquely defined by the Galerkin formulation. That expression of the Coriolis matrix is naturally skew-symmetric and does not require any reconstruction for the tangential velocity component (Walters et al., submitted for publication). The total number of degrees of freedom for the $P_1^{NC} - P_1$ and RT_0 schemes is equal to $N_V + 2N_S \approx \frac{7}{2}N_E$ and $N_E + N_S \approx \frac{5}{2}N_E$, respectively.

It should be noted that all the integrals in the weak formulation could have been computed on a partition of Ω into subdomains Ω_e corresponding to the elements of the triangulation.
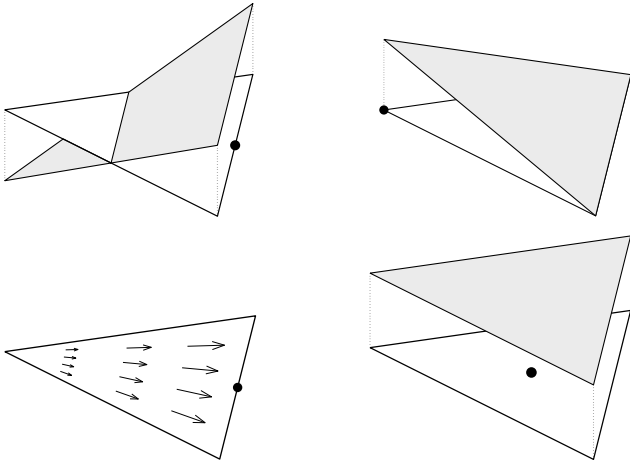

Fig. 1. $P_1^{NC} - P_1$ (top) and RT_0 (bottom) shape functions. The velocity shape functions are shown on the left and the elevation shape functions are shown on the right. The node associated to each of them is represented by "●". Velocity shape functions are scalar for $P_1^{NC} - P_1$ and vectorial for RT_0.

This would amount to define $\langle . \rangle = \sum_e \int_{\Omega_e} . \, d\Omega$ and $\ll . \gg = \sum_e \int_{\partial \Omega_e} . \, d\Gamma$. Although this would not change formulations (5) and (6) as all the terms in these equations are continuous, it would lead to a different expression of the discrete Eqs. (7) and (8). In that case, the use of the Gauss theorem would introduce inter-element fluxes that are not uniquely defined as some of the discrete variables can be discontinuous between elements. A unique expression of the inter-element fluxes could be obtained by adding continuity constraints to the weak formulation. These constraints, which vanish in the continuous case, can be applied to the model variables or to some combination of these variables, like Riemann invariants. As a result, several discrete formulations can be obtained. Computing the weak formulation on the partition of Ω is required as soon as the problem is non-linear (see for instance Hanert et al., 2005 or Danilov et al., in press). For a linear problem, the discrete formulation (7) and (8) is however sufficient although it has some limitations. Some of these limitations are discussed in Section 5.

Eqs. (7) and (8) are finally discretized in time by using an implicit θ-scheme for the divergence, Coriolis and gradient terms, and an explicit scheme for the remaining terms. The fully discrete equations then read

$$M_{ij}^\eta \frac{E_j^{n+1} - E_j^n}{\Delta t} + D_{ij}(\alpha U_j^{n+1} + (1 - \alpha)U_j^n) = 0 \qquad (9)$$

$$M_{ij}^u \frac{U_j^{n+1} - U_j^n}{\Delta t} + C_{ij}(\beta U_j^{n+1} + (1 - \beta)U_j^n)$$
$$= -G_{ij}(\gamma E_j^{n+1} + (1 - \gamma)E_j^n) + R_j^n, \qquad (10)$$

where α, β and γ represent the degree of implicity of the time discretization of the divergence, Coriolis and gradient terms, respectively. Other time integration could also have been used, like the explicit third order Adams–Bashforth and fourth order Runge–Kutta schemes. These schemes being explicit, the model efficiency could then be enhanced by lumping either the elevation mass matrix (for $P_1^{NC} - P_1$) or the velocity mass matrix (for RT_0) in order to avoid having to solve a non-diagonal system of equations. Lumping the RT_0 velocity mass matrix or the $P_1^{NC} - P_1$ elevation mass matrix has a small impact on the accuracy of the solution as long as the mesh resolution is not too coarse (Le Roux et al., in press).

3. Propagation factor

Although the $P_1^{NC} - P_1$ and RT_0 are known to have good dispersive properties, most dispersion analysis of these elements have either followed a purely numerical or a purely analytical approach. The former usually amounts to numerically simulate different types of waves and see how a method performs for different meshes and timestepping schemes. The latter is usually based on a Fourier analysis of the space-discretized but time-continuous equations expressed on a uniform mesh. In this section, we consider a third approach, which somehow lies between the two previous ones. It consists in numerically computing the propagation factor of the fully discrete equations obtained with both schemes on arbitrary meshes.

The complex propagation factor has been introduced by Leendertse (1967) and later used by Gray and Lynch (1977) and Kinnmark and Gray (1984) to evaluate the ability of a numerical scheme to accurately represent the amplitude and phase speed of a wave. If we introduce the parameters $\lambda = e^{i\omega\Delta t}$ and $\lambda_{ex} = e^{i\omega_{ex}\Delta t}$, where ω is the computed wave frequency and ω_{ex} is the analytical wave frequency, we can define the complex propagation factor T as

$$T = \left(\frac{\lambda}{\lambda_{ex}}\right)^N,$$

where $N = \frac{2\pi}{\omega_{ex}\Delta t}$ is the number of time steps required for the analytical wave to propagate one wavelength.

The propagation factor is the ratio of the computed wave over the analytical wave after the time required for the analytical wave to propagate one time step. The magnitude of T therefore represents the relative change in the wave amplitude due to the numerical scheme. The argument of T is the phase lag of the computed wave compared to the analytical wave and is a measure of the relative celerity and the computed and analytical waves.

To numerically compute the propagation factor for waves with different wave numbers, we follow the approach suggested by Bernard et al. (2008). By considering oscillatory solutions of the form $E^{n+1} = \lambda E^n$ and $U^{n+1} = \lambda U^n$, the system of Eqs. (9) and (10) can be recast as

$$\lambda \underbrace{\begin{pmatrix} M^\eta & \alpha\Delta t D \\ \gamma\Delta t G & M^u + \beta\Delta t C \end{pmatrix}}_{\equiv A} \begin{pmatrix} E^n \\ U^n \end{pmatrix} = \underbrace{\begin{pmatrix} M^\eta & -(1-\alpha)\Delta t D \\ -(1-\gamma)\Delta t G & M^u - (1-\beta)\Delta t C \end{pmatrix}}_{\equiv B} \begin{pmatrix} E^n \\ U^n \end{pmatrix},$$

which shows that the set of admissible discrete values of λ is the eigenvalues spectrum of the matrix $A^{-1}B$. With each eigenvalue λ_j, we can then associate an elevation eigenmode E_j and compute its Fourier transform. The two components of the wave vector of the mode E_j then correspond to the maximum of its power spectrum. As a result, a wave vector (k_j, l_j) can be associated with each eigenvalue λ_j, which in turn can be used to compute the corresponding propagation factor value T_j.

Computing the propagation factor numerically allows us to use non-uniform and non-periodic meshes, with any kind of boundary conditions. In that respect, numerical calculations are more flexible than the usual analytical ones but lack the generality of the exact analysis. In that respect, it should be noted that the analytical dispersion relations of the $P_1^{NC} - P_1$ and RT_0 elements have been computed analytically by Le Roux et al. (2007) and Le Roux and Pouillot (2008) for gravity and Rossby waves, respectively.

In the present work, we have computed the propagation factor on square domain that is periodic in the x-direction and bounded in the y-direction. No-normal flow boundary conditions are therefore imposed on the upper and lower boundaries. The water depth is assumed constant. Calculations have been performed on structured meshes made of equilateral triangles and on unstructured meshes. In each case, the meshes were composed of 288 triangles. Two values of the time step have been selected, one that satisfies the CFL condition associated with gravity waves and one that does not. By using a non-constant Coriolis parameter, Eqs. (1) and (2) allow the existence of both fast inertia–gravity waves and slow Rossby waves. Thanks to the large difference in the frequency values between these two types of waves, they can easily be distinguished and the propagation factor can be computed for each of them. Results are shown as contour plots of the amplitude and argument of the propagation factor as functions of the product of the wavenumbers k and l with the mesh size d. Since the largest value of k and l is π/d, the range of kd and ld is limited to $[0, \pi]$. Note that a mesh averaged value of d is used for unstructured meshes. A continuous representation of the propagation factor is obtained by interpolating between the discrete values T_j.

In Fig. 2, we show the amplitude of the propagation factor obtained for the $P_1^{NC} - P_1$ and RT_0 schemes with a semi-implicit ($\alpha = \beta = \gamma = 1/2$) and fully-implicit ($\alpha = \beta = \gamma = 1$) time integration scheme. In each case, results are obtained for gravity waves on a uniform mesh of equilateral triangles and with a time step satisfying the gravity waves CFL condition $\left(\Delta t = \frac{d}{5\sqrt{gh}}\right)$. The amplitude of the propagation factor is similar for both schemes and the well-known dissipative behaviour of fully-implicit models is observed.
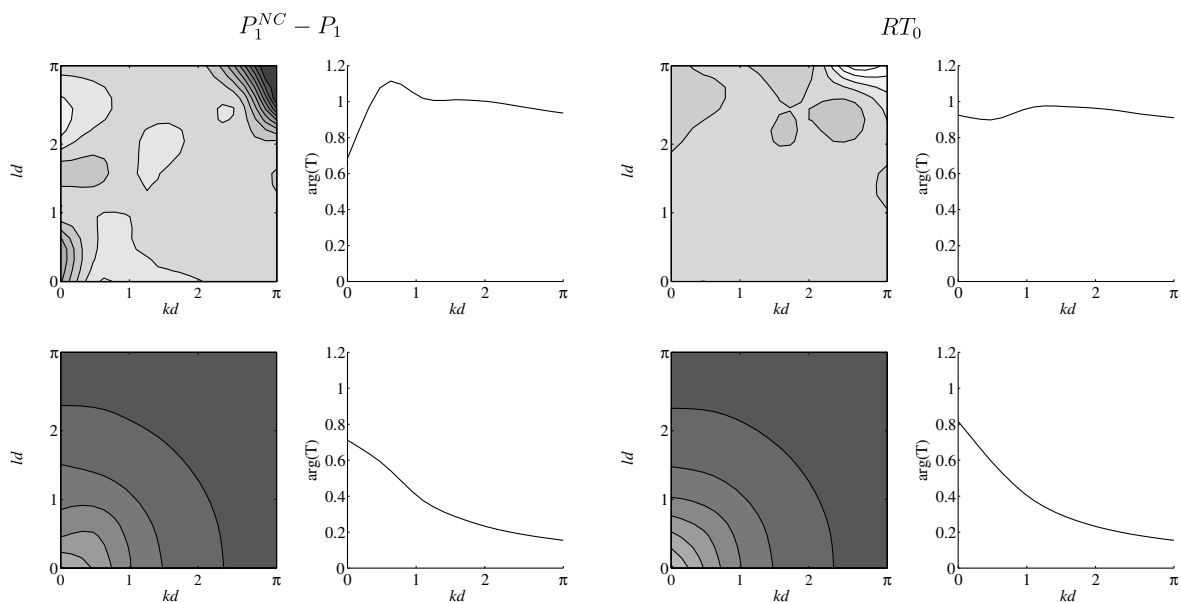
$$P_1^{NC} - P_1 \qquad\qquad RT_0$$
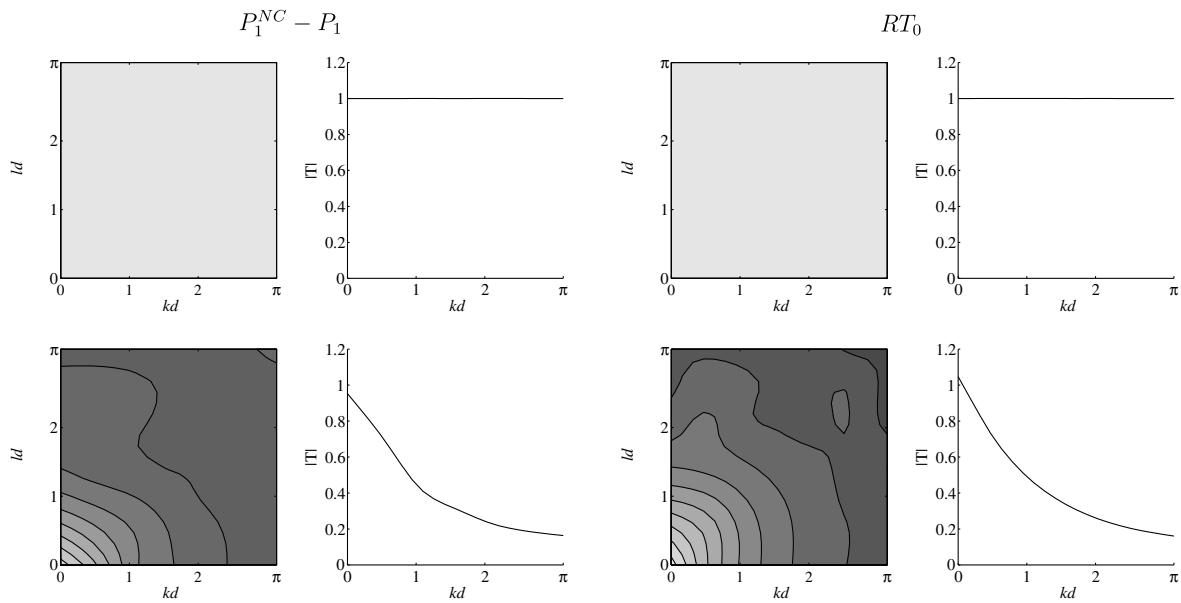
Fig. 2. Amplitude of the propagation factor ($|T|$) of inertia–gravity waves for the $P_1^{NC} - P_1$ and RT_0 schemes with semi-implicit (top) and fully-implicit (bottom) time integration. Calculations are done on an uniform mesh of equilateral triangles and the time step is set to $\Delta t = \frac{d}{5\sqrt{gh}}$. For each subplot, the left panel represents $|T|$ as a function of kd and ld. The contour interval is set to 0.1. The right panel represents $|T|$ as a function of kd for $ld = 0$.

In Fig. 3, we show the argument of the propagation factor obtained for both finite element schemes. For these experiments, we have only considered a semi-implicit time integration scheme and investigated the effect of the time step value on the dispersion of inertia–gravity waves. Calculations are performed on an unstructured mesh. When using a time step small enough to satisfy the gravity waves CFL condition, the argument of T is close to one for both finite element pairs, which shows that they both propagate accurately fast inertia–gravity waves. When the time step exceeds the CFL condition, small wavelength waves are significantly slowed down. Although both models are performing well, the RT_0 appears to propagate gravity waves more accurately, at all wavelengths.

The same analysis can be performed for Rossby waves (Fig. 4). In that case, the time step has almost no influence as Rossby waves are much slower that inertia–gravity waves and thus evolve on a larger time scale. As a result, the CFL condition based on the speed of gravity waves no more acts as a threshold above which waves are being slowed down. It can be seen that both schemes give qualitatively similar results and accurately represent the propagation of these waves. The main discrepancies are observed for small wavelengths for which both schemes tend to underestimate Rossby waves velocity by about 30%.

Finally, it should be mentioned that the same analysis can be performed when both schemes are lumped. It is then observed that both the $P_1^{NC} - P_1$ and RT_0 schemes are still accurately

$$P_1^{NC} - P_1 \qquad\qquad RT_0$$

Fig. 3. Argument of the propagation factor (arg(T)) of inertia–gravity waves for the $P_1^{NC} - P_1$ and RT_0 schemes with semi-implicit time integration. The time step is set to $\Delta t = \frac{d}{5\sqrt{gh}}$ (top) and $\Delta t = \frac{5d}{\sqrt{gh}}$ (bottom). Calculations are performed on an unstructured mesh. For each subplot, the left panel represents arg(T) as a function of kd and ld with a contour interval equal to 0.1. The right panel represents arg(T) as a function of kd for $ld = 0$.
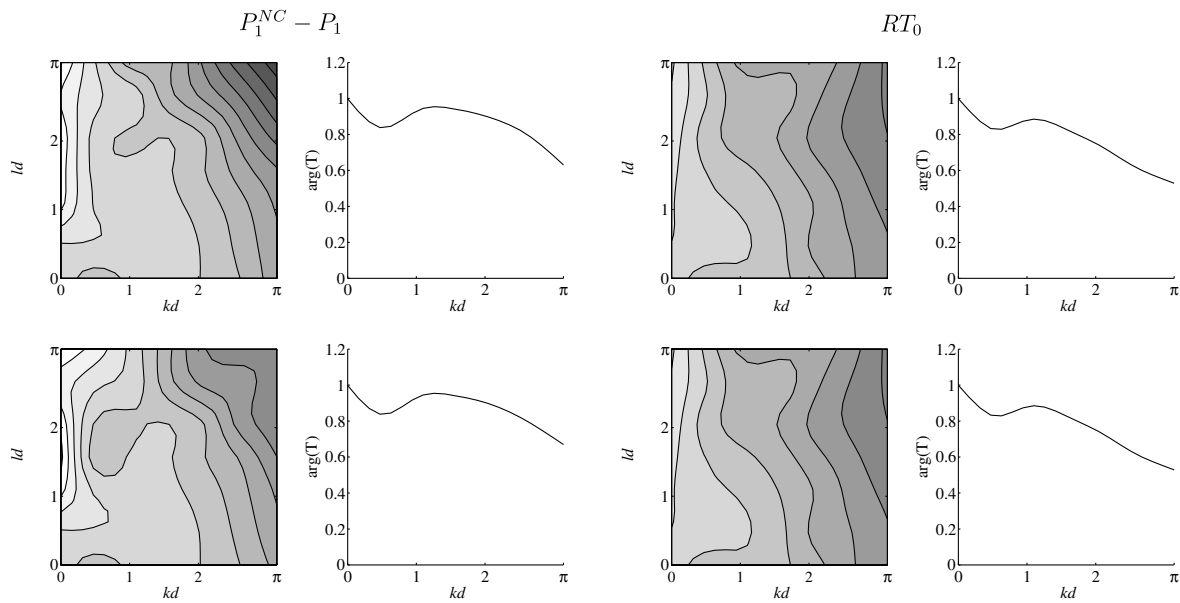
$$P_1^{NC} - P_1 \qquad\qquad\qquad RT_0$$

Fig. 4. Argument of the propagation factor as in Fig. 3 but for Rossby waves.

representing inertia–gravity and Rossby waves. As observed by Le Roux et al. (in press), the lumped $P_1^{NC} - P_1$ scheme tends to underestimate the inertia–gravity waves propagation speed by at most 25% for wavelengths smaller than $4d$. This is not observed for the lumped RT_0, which still very accurately represents all wavelengths. In the case of Rossby waves, the effect of mass lumping is negligible and no changes in the amplitude or propagation speed are observed.

4. Conservation and consistency

One of the most significant differences between the RT_0 and $P_1^{NC} - P_1$ element is the discretization of the continuity equation and the subsequent requirements for consistency with the scalar transport equation. For purely hydrodynamic calculations with (1) and (2), this is not an issue. However, for passive scalar transport or baroclinic calculations, this choice presents a significant consideration.

For the RT_0 element, the elevation test function is a constant on each element. Hence the continuity equation, the first equation in (6), can be written in a finite volume form by converting the flux divergence term into a line integral around an element Ω_e:

$$A_e \frac{d\eta_e}{dt} = \int_{\Omega_e} \nabla \cdot (h\mathbf{u}^h) d\Omega = \int_{\partial\Omega_e} h\mathbf{u}^h \cdot \mathbf{n} d\Gamma, \qquad (11)$$

where A_e is the area of Ω_e and $\partial\Omega_e$ are the edges for that element.

For the $P_1^{NC} - P_1$ element, the test function is a linear conforming (P_1) representation (see Fig. 1). After the global integration in (5) or (6), this function can be represented as a hat function which is unity at a particular vertex and zero at the adjacent vertices. Hence continuity is satisfied in a weighted-residual sense in the support for a particular vertex. This element does not therefore naturally satisfy continuity on an element by element basis. However, an elementwise continuity equation can be recovered by defining the thickness fluxes between elements as being equal to the contribution of the other mesh elements (Hughes et al., 2000; Berger and Howington, 2002).

Consistency requires that for a constant value of the scalar variable the discretized continuity equation and the scalar transport equation are identical (Gross et al., 2002; White et al., 2008b).

Otherwise there will be spurious sources and sinks for the scalar variable and the solution will not necessarily converge.

As a result, finite volume scalar transport approximations can be used with the RT_0 formulation with access to the large body of knowledge that has been developed for these methods (see for instance Durran, 1999). In particular, methods are available to solve for advection-dominated flows as represented by the Euler equation. This class of problems is important in many geophysical flows of interest.

On the other hand, continuous Galerkin methods must be used with the $P_1^{NC} - P_1$ element. That is, the scalar transport equation is solved in the same weighted-residual form about each vertex. These methods generally work well when the scalar variable field is smooth. However, they tend to produce over and undershoots when there are abrupt changes in the magnitude of the scalar variable (see for instance Hanert et al., 2004). Moreover, it is problematic trying to construct robust advection approximations for these schemes.

In the end, consistency requirements present another criterion to apply in choosing between these two elements. Ultimately, the particular problem under consideration has a strong influence on the choice.

5. Convergence analysis

In this section, we compare the convergence rates of both FE schemes by solving the steady Stommel problem. This problem amounts to find the steady state solution of the linearised Eqs. (1) and (2) on a beta plane ($f = f_0 + \beta_0 y$) with linear bottom friction and wind stress. The Stommel problem analyses the balance between the Coriolis force, bottom drag and wind stress. In a closed domain with an anti-cyclonic wind-stress, the resulting flow is equatorwards in the interior of the domain. The equatorwards flow is exactly balanced by a more intense polewards flow in the western boundary layer. In the western boundary layer, the balance is principally between the bottom friction and the beta effect. A length scale for the boundary layer width can then be obtained by taking the ratio between the linear friction and beta coefficients (see for instance Vallis, 2006).

An analytical solution of the steady Stommel problem has been derived by Mushgrave (1985) and can be used to compute the

discretization error. Fig. 5 shows the L_2-error on the elevation and velocity for different mesh resolutions. Calculations have been performed on structured uniform and unstructured meshes. The model equations have been solved on the domain $[0,L] \times [0,L]$ where $L = 10^6$ m. The parameters f_0, β_0 and h are equal to 10^{-4} s^{-1}, 10^{-11} m^{-1} s^{-1} and 1000 m, respectively. The forcing and dissipation terms have the following expression: $\mathcal{T} = 0.2 \sin(y - L/2)\mathbf{e}_x$ kg m^{-1} s^{-2} and $\mathcal{D} = \gamma\mathbf{u}$, where $\gamma = 10^{-5}$ s^{-1}.

The rate of convergence in the L_2-norm is theoretically expected to be quadratic for $P_1^{NC} - P_1$ and linear for RT_0 as the elevation is only piecewise constant for that element. These rates of convergence are indeed observed on a structured uniform mesh. The same results are observed on an unstructured mesh with the exception that the convergence rate of the velocity with the $P_1^{NC} - P_1$ scheme is only linear. This drop in the order of convergence of the $P_1^{NC} - P_1$ scheme that is observed as soon as the mesh is not uniform seems to indicate that there is a shortcoming in the discrete formulation used. It might be due to the Continuous Galerkin approach that has been followed to derive the discrete equations. Indeed, the discrete P_1^{NC} velocity is discontinuous between elements except at mid-segments. Therefore, one may question the use of a Continuous Galerkin method to derive the discrete equations as this method does not introduce fluxes between elements as it is required for fully discontinuous approximations. In particular, for such approximations the discrete divergence term should be expressed as

$$\int_\Omega \boldsymbol{\nabla} \cdot (h\mathbf{u}^h)\psi_i \mathrm{d}\Omega = \sum_{e=1}^{N_E} \int_{\Omega_e} \boldsymbol{\nabla} \cdot (h\mathbf{u}^h)\psi_i \mathrm{d}\Omega$$

$$= \underbrace{\sum_{e=1}^{N_E} \int_{\partial\Omega_e} h\mathbf{u}^h \cdot \mathbf{n}_e \psi_i \mathrm{d}\Gamma}_{\neq 0} - \sum_{e=1}^{N_E} \int_{\Omega_e} h\mathbf{u}^h \cdot \boldsymbol{\nabla}\psi_i \mathrm{d}\Omega,$$

where $\mathbf{n}_e$ is the outward normal vector to $\partial\Omega_e$. The boundary integral in that expression is usually different from zero as $\mathbf{u}^h$ is discontinuous between elements. However, it is neglected in the weak formulation (5) used to derive the discrete $P_1^{NC} - P_1$ continuity equation. By doing so, one constrains the discrete velocity field to be such that the thickness flux is continuous between elements. Such a constraint on the velocity might be the cause of the observed decrease in the convergence rate.

As mentioned by Legat and coworkers (personal communication), the $P_1^{NC} - P_1$ scheme should indeed be derived by following a Discontinuous Galerkin approach, which would introduce fluxes between elements. An exact or approximate Riemann solver would then be needed to compute these fluxes. Such an approach might allow to recover the quadratic rate of convergence on non-uniform meshes and improve the stability of the scheme. However, the computational cost of the scheme is also likely to be substantially increased because of these additional fluxes involving solution values in adjacent elements. A similar approach to improve the current $P_1^{NC} - P_1$ formulation could be to apply the interface stabilisation method suggested by Labeur and Wells (2007).
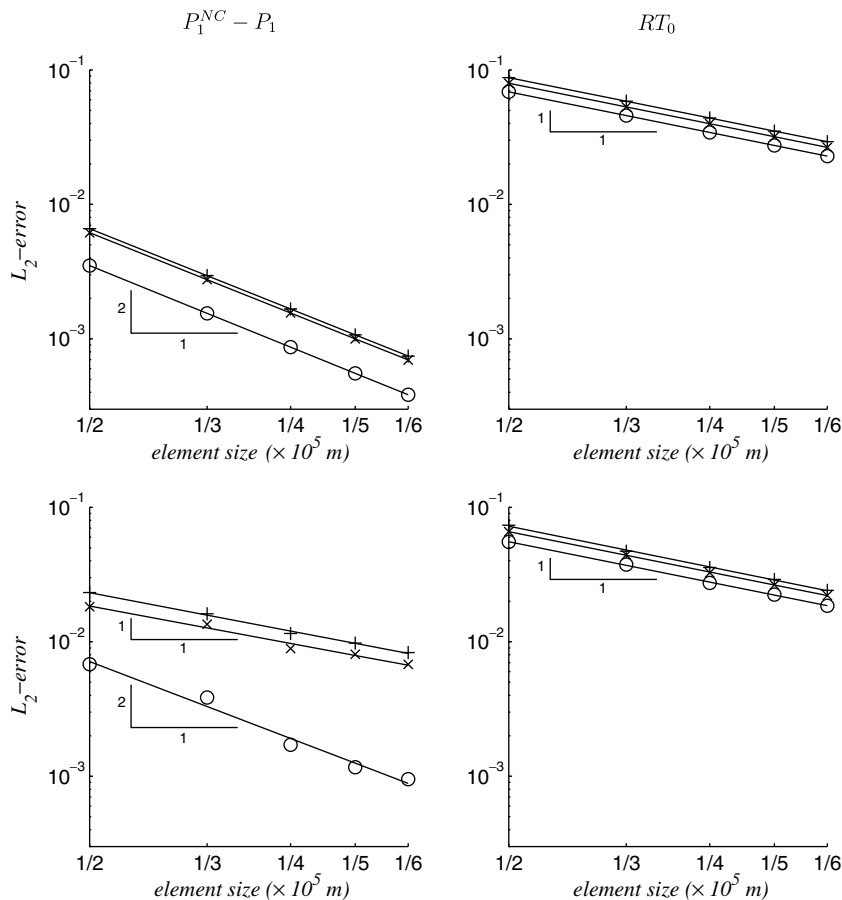

Fig. 5. Convergence analysis for the $P_1^{NC} - P_1$ and RT_0 schemes on structured uniform (top) and unstructured (bottom) meshes. The elevation, and x- and y-components of the velocity error curves are represented by "○", "×" and "+" symbols, respectively.

6. Numerical example: Stommel problem

In this section, we present a numerical illustration of the effect that the placement of local variables within an element can have on the accuracy of the solution. The RT_0 and $P_1^{NC} - P_1$ element differ in the sense that the former has only one velocity degree of freedom per segment while the latter has two. As a result, when imposing the no-normal flow boundary condition, all the RT_0 velocity nodal values that are on the boundary have to be set to zero. This is however not the case with the $P_1^{NC} - P_1$ scheme as only one of the two boundary velocity degrees of freedom is constrained when boundary conditions are imposed strongly. This suggests that the $P_1^{NC} - P_1$ scheme might be more accurate to simulate flows presenting boundary layer, especially when the mesh resolution is coarse compared to the boundary layer width.

As an illustration, we consider the solution of the transient non-linear Stommel problem. The computational domain and experiment setup is the same as in Section 5 except that the problem is now non-linear and time dependent. The non-linear terms both the RT_0 and $P_1^{NC} - P_1$ schemes are discretized by following a similar approach as in Hanert et al. (2005). The physical parameters have the same values as in Section 5 with the exception of the linear bottom drag coefficient (γ) which is now equal to 10^{-7} s^{-1} in order to have a more intense western boundary layer. The mesh is structured with a uniform resolution of about 30 km. The time integration scheme is semi-implicit for the linear terms and explicit for the non-linear ones. The time step is set to 10^3 s.

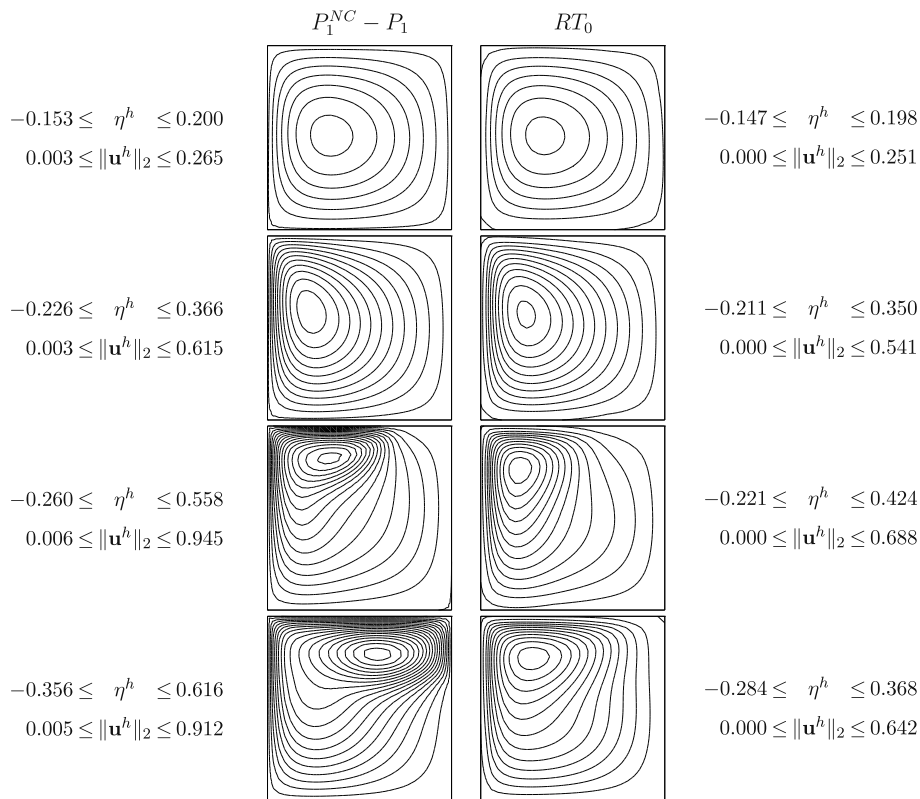The elevation field obtained with both schemes after 10^6, 2×10^6, 4×10^6 and 6×10^6 s is shown in Fig. 6. At the beginning of the simulation, the flow velocity is quite weak and the main driving mechanisms are the wind, friction and beta effect. As the flow in the boundary layer intensifies, non-linear terms become more important and tend to advect the vorticity of the gyre polewards. The center of the gyre therefore moves polewards, which results in an intensification of the current in the poleward half and a weakening in the equatorward half. The importance of that polewards displacement of the gyre's center obviously depends on the magnitude of the velocity in the boundary layer.

Since the $P_1^{NC} - P_1$ has an unconstrained tangential velocity degree of freedom on the boundary, it is able to represent quite accurately the velocity field in the boundary layer despite the coarse mesh resolution. The RT_0 scheme, on the other hand, does not have any tangential velocity degree of freedom on the boundary. The closest velocity nodal value is at a distance $d/2$ from the boundary, where d is the mesh resolution. As a result, non-linear terms have a stronger effect with the $P_1^{NC} - P_1$ model than with the RT_0 model. As can be seen from Fig 6, the RT_0 solution seems to start lagging behind the $P_1^{NC} - P_1$ solution as soon as the boundary layer develops. As time increases, the difference between both solutions also increases and leads to totally different results.

7. Conclusions

The $P_1^{NC} - P_1$ and RT_0 finite element pairs have been known for some time to be good elements to solve the shallow water equations. Previous studies have shown that these elements were free of spurious computational modes and had good dispersion properties for both inertia–gravity and Rossby waves. However, the reasons for selecting one element rather than the other were less clear and were generally due to personal preferences or previous experience with the finite element or finite volume/difference methods. In this work, we have tried to highlight the differences between these two elements in order to propose more quantitative selection criteria. The main conclusion that we can draw is that the

$P_1^{NC} - P_1$　　　　　　RT_0

$-0.153 \leq \quad \eta^h \quad \leq 0.200$
$0.003 \leq \|\mathbf{u}^h\|_2 \leq 0.265$

$-0.147 \leq \quad \eta^h \quad \leq 0.198$
$0.000 \leq \|\mathbf{u}^h\|_2 \leq 0.251$

$-0.226 \leq \quad \eta^h \quad \leq 0.366$
$0.003 \leq \|\mathbf{u}^h\|_2 \leq 0.615$

$-0.211 \leq \quad \eta^h \quad \leq 0.350$
$0.000 \leq \|\mathbf{u}^h\|_2 \leq 0.541$

$-0.260 \leq \quad \eta^h \quad \leq 0.558$
$0.006 \leq \|\mathbf{u}^h\|_2 \leq 0.945$

$-0.221 \leq \quad \eta^h \quad \leq 0.424$
$0.000 \leq \|\mathbf{u}^h\|_2 \leq 0.688$

$-0.356 \leq \quad \eta^h \quad \leq 0.616$
$0.005 \leq \|\mathbf{u}^h\|_2 \leq 0.912$

$-0.284 \leq \quad \eta^h \quad \leq 0.368$
$0.000 \leq \|\mathbf{u}^h\|_2 \leq 0.642$

Fig. 6. Elevation field after 10^6, 2×10^6, 4×10^6 and 6×10^6 s (from top to bottom), obtained with $P_1^{NC} - P_1$ and RT_0 models of the non-linear Stommel problem. The contour interval is set to 0.05 m. Minimum and maximum values of the elevation (in m) and norm of the velocity (in ms^{-1}) are given at each stage. Note that for RT_0, the piecewise constant elevation field has been interpolated on the vertices to produce the figures.

choice between elements is highly application dependent. For purely hydrodynamic problems, the $P_1^{NC} - P_1$ generally provides greater accuracy. This element may be used for applications with scalar transport, but continuous methods must be used to maintain consistency. On the other hand, the RT_0 element leads to a finite volume approximation of the continuity and scalar transport equations which may be more appropriate for certain applications.

For applications where the simulation of tracers transport is not required, the consistency of the tracer equation with the continuity equation is not an issue. In that case, the $P_1^{NC} - P_1$ element has the advantage of having more degrees of freedom than RT_0 and a better placement of these degrees of freedom over an element. The use of full velocity rather than normal velocity nodal values on each segment allows for a more accurate representation of inertial boundary layer flows even with rather coarse meshes. Although the finite element formulation used in this work could be improved, the $P_1^{NC} - P_1$ scheme is more accurate than the RT_0 scheme in the L_2-norm and has at least the same convergence rate.

For applications that require the simulation of tracers transport, the consistency constraint renders the RT_0 more attractive. This is due to the finite volume form of the continuity equation that allows the use of a large variety of finite volume scalar advection schemes, some of which have proved to be quite accurate for advection-dominated flows. For the $P_1^{NC} - P_1$ element, the finite element formulation of the continuity equation combined with the use of a piecewise linear approximation of the elevation involves the use of P_1 tracer advection schemes, which could be inaccurate for advection-dominated flows.

Finally, we would like to stress that the present comparison has been carried out only for 2D shallow water problems. Additional difficulties are to be expected when solving the 3D primitive equations, which may result in additional selection criteria. In the three-dimensional case, the consistency constraint requires the horizontal discretization of the vertical velocity to be identical to the one of the surface elevation (see for instance White et al., 2008b). This leads to the use of P_1 and P_0 horizontal discretizations of the vertical velocity in 3D models based on the $P_1^{NC} - P_1$ and RT_0 elements, respectively. The use of a P_1 vertical velocity could have a significant detrimental effect on the model efficiency while a P_0 vertical velocity is not well suited for representing upwelling in unresolved boundary layers. The latter can result in a patchy vertical velocity (Danilov, personal communication). Further work should therefore be undertaken to extend the present comparison to three-dimensional problems.

Acknowledgements

References

Adcroft, A.J., Hill, C.N., Marshall, J.C., 1999. A new treatment of the Coriolis terms in C-grid models at both high and low resolutions. Monthly Weather Review 127 (8), 1928–1936.

Berger, R.C., Howington, S.E., 2002. Discrete fluxes and mass balance in finite elements. Journal of Hydraulic Engineering 87, 87–92.

Bernard, P.-E., Chevaugeon, N., Legat, V., Deleersnijder, E., Remacle, J.-F., 2007. High-order h-adaptive discontinuous Galerkin methods for ocean modeling. Ocean Dynamics 57, 109–121.

Bernard, P.-E., Remacle, J.-F., Legat, V., Deleersnijder, E., 2008. Dispersion analysis of discontinuous Galerkin schemes applied to Poincaré, Kelvin and Rossby waves. Journal of Scientific Computing 34, 26–47.

Casulli, V., Walters, R.A., 2000. An unstructured grid, three-dimensional model based on the shallow water equations. International Journal for Numerical Methods in Fluids 32, 331–348.

Chen, C., Liu, H., Beardsley, R.C., 2003. An unstructured grid, finite-volume, three-dimensional, primitive equations ocean model: applications to coastal ocean and estuaries. Journal of Atmospheric and Oceanic Technology 20, 159–186.

Danilov, S., Kivman, G., Schröter, J., in press. Modeling ocean circulation on unstructured meshes: comparison of two horizontal discretizations. Ocean Dynamics.

Durran, D.R., 1999. Numerical Methods for Wave Equations in Geophysical Fluid Dynamics. Texts in Applied Mathematics. Springer.

Fringer, O.B., Gerritsen, M., Street, R.L., 2006. An unstructured-grid, finite-volume, nonhydrostatic, parallel coastal ocean simulator. Ocean Modelling 14, 139–173.

Giraldo, F.X., Warburton, T., 2008. A high-order triangular discontinuous Galerkin oceanic shallow water model. International Journal for Numerical Methods in Fluids 56, 899–925.

Gray, W.G., Lynch, D.R., 1977. Time-stepping schemes for finite element tidal model computations. Advances in Water Resources 1, 83–95.

Greenberg, D.A., Dupont, F., Lyard, F., Lynch, D.R., Werner, F.E., 2007. Resolution issues in numerical models of oceanic and coastal circulation. Continental Shelf Research 27, 1317–1343.

Gross, E.S., Bonaventura, L., Rosatti, G., 2002. Consistency with continuity in conservative advection schemes for free-surface modes. International Journal for Numerical Methods in Fluids 38, 307–327.

Ham, D.A., Pietrzak, J., Stelling, G.S., 2005. A scalable unstructured grid 3-dimensional finite volume model for the shallow water equations. Ocean Modelling 10, 153–169.

Hanert, E., Le Roux, D.Y., Legat, V., Deleersnijder, E., 2004. Advection schemes for unstructured grid ocean modelling. Ocean Modelling 7, 39–58. doi:10.1016/S1463-5003(03)00029-5.

Hanert, E., Le Roux, D.Y., Legat, V., Deleersnijder, E., 2005. An efficient Eulerian finite element method for the shallow water equations. Ocean Modelling 10, 115–136. doi:10.1016/j.ocemod.2004.06.006.

Hanert, E., Legat, V., 2006. How to save a bad element with weak boundary conditions. Computers and Fluids 35, 477–484. doi:10.1016/j.compfluid.2005.02.005.

Hanert, E., Legat, V., Deleersnijder, E., 2003. A comparison of three finite elements to solve the linear shallow water equations. Ocean Modelling 5, 17–35. doi:10.1016/S1463-5003(02)00012-4.

Hua, B.L., Thomasset, F., 1984. A noise-free finite element scheme for the two-layer shallow water equations. Tellus 36A, 157–165.

Hughes, T.J.R., Engel, G., Mazzei, L., Larson, M.G., 2000. The continuous Galerkin method is locally conservative. Journal of Computational Physics 163, 467–488.

Kinnmark, I.P., Gray, W.G., 1984. A two-dimensional analysis of the wave equation model for finite element tidal computations. International Journal for Numerical Methods in Engineering 20, 369–383.

Kolar, R.L., Westerink, J.J., Cantekin, M.E., Blain, C., 1994. Aspects of nonlinear simulations using shallow water models based on the wave continuity equation. Computers and Fluids 23, 523–538.

Labeur, R.J., Wells, G.N., 2007. A galerkin interface stabilisation method for the advection-diffusion and incompressible Navier–Stokes equations. Computer Methods in Applied Mechanics and Engineering 196, 4985–5000.

Lambrechts, J., Hanert, E., Deleersnijder, E., Bernard, P.-E., Legat, V., Remacle, J.-F., Wolanski, E., 2008. A multi-scale model of the hydrodynamics of the whole Great Barrier Reef. Estuarine, Coastal and Shelf Science 79, 143–151. doi:10.1016/j.ecss.2008.03.016.

Le Roux, D.Y., 2005. Analysis of the $P_1^{NC} - P_1$ finite-element pair in shallow-water ocean models. SIAM Journal of Scientific Computing 27, 394–414.

Le Roux, D.Y., Hanert, E., Rostand, V., Pouillot, B., in press. Effect of mass lumping on gravity and Rossby waves in 2D finite-element shallow-water models. International Journal for Numerical Methods in Fluids. doi:10.1002/fld.1837.

Le Roux, D.Y., Pouillot, B., 2008. Analysis of numerically-induced oscillations in 2D finite-element shallow-water models. SIAM Journal of Scientific Computing 30, 1971–1991.

Le Roux, D.Y., Rostand, V., Pouillot, B., 2007. Analysis of numerically-induced oscillations in 2D finite-element shallow-water models. Part I: inertia–gravity waves. SIAM Journal of Scientific Computing 29, 331–360.

Leendertse, J.J., 1967. Aspects of a computational model for long period water-wave propagation. Tech. Rep. RM-5294-PR, Santa Monica, Rand Memorandum.

Lynch, D.R., Gray, W.G., 1979. A wave equation model for finite-element tidal computations. Computers and Fluids 7, 207–228.

Massey, T.C., Blain, C.A., 2006. In search of a consistent and conservative mass flux for the gwce. Computer Methods in Applied Mechanics and Engineering 195, 571–587.

Miglio, E., Quarteroni, A., Saleri, F., 1999. Finite element approximation of quasi-3D shallow water equations. Computer Methods in Applied Mechanics and Engineering 174, 355–369.

Mushgrave, D.L., 1985. A numerical study of the roles of subgyre-scale mixing and the western boundary current on homogenization of a passive tracer. Journal of Geophysical Research 90, 7037–7043.

Raviart, P.A., Thomas, J.M., 1977. A mixed finite element method for 2nd order elliptic problems. In: Galligani, I., Magenes, E. (Eds.), Mathematical Aspects of the Finite Element Methods, Lecture Notes in Mathematics. Springer-Verlag, pp. 292–315.

Sobolev, S.V., Babeyko, A.Y., Wang, R., Hoechner, A., Galas, R., Rothacher, M., Sein, D.V., Schroeter, J., Lauterjung, J., Subarya, C., 2007. Tsunami early warning using GPS-shield arrays. Journal of Geophysical Research B: Solid Earth 112 (8). art. no. B08415.

Stuhne, G.R., Peltier, W.R., 2006. A robust unstructured grid discretization for 3-dimensional hydrostatic flows in spherical geometry: a new numerical structure for ocean general circulation modeling. Journal of Computational Physics 213, 704–729.

Vallis, G.K., 2006. Atmospheric and Oceanic Fluid Dynamics: Fundamentals and Large-scale Circulation. Cambridge University Press.

Walters, R.A., 1983. Numerically induced oscillations in finite element approximations to the shallow water equations. International Journal for Numerical Methods in Fluids 3, 591–604.

Walters, R.A., 2005. Coastal ocean models: two useful finite element methods. Continental Shelf Research 25, 775–793.

Walters, R.A., Carey, G.F., 1983. Analysis of spurious oscillations modes for the shallow water and Navier–Stokes equations. Computers and Fluids 11, 51–68.

Walters, R.A., Carey, G.F., 1984. Numerical noise in ocean and estuarine models. Advances in Water Resources 7, 15–20.

Walters, R.A., Casulli, V., 1998. A robust, finite element model for hydrostatic surface water flows. Communications in Numerical Methods in Engineering 14, 931–940.

Walters, R.A., Pietrzak, J., Hanert, E., Le Roux, D.Y., submitted for publication. Solution of the shallow water equations using unstructured staggered grids. Ocean Modelling.

White, L., Deleersnijder, E., Legat, V., 2008a. A three-dimensional unstructured mesh finite element shallow-water model, with application to the flows around an island and in a wind-driven, elongated basin. Ocean Modelling 22, 26–47.

White, L., Legat, V., Deleersnijder, E., 2008b. Tracer conservation for three-dimensional, finite element, free-surface, ocean modeling on moving prismatic meshes. Monthly Weather Review 136, 420–442.